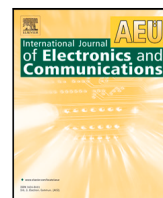




Contents lists available at ScienceDirect

Int. J. Electron. Commun. (AEÜ)

journal homepage: [www.elsevier.com/locate/aeue](http://www.elsevier.com/locate/aeue)

Regular paper

# Low-profile dual-band implantable antenna for compact implantable biomedical devices<sup>☆</sup>

Muath Al-Hasan<sup>a,\*</sup>, Penchala Reddy Sura<sup>b</sup>, Amjad Iqbal<sup>c</sup>, Jun Jiat Tiang<sup>c</sup>, Ismail Ben Mabrouk<sup>d</sup>, Mourad Nedil<sup>e</sup>

<sup>a</sup> Network and Communications Engineering Department, Al Ain University, Al Ain, United Arab Emirates

<sup>b</sup> Department of ECE, Visvodaya Engineering College, Kavali 524201, India

<sup>c</sup> Faculty of Engineering, Multimedia University, Cyberjaya, Malaysia

<sup>d</sup> Department of Engineering, Durham University, Durham DH1 3LE, UK

<sup>e</sup> Communications Research Laboratory (LRTCS), University of Quebec at Abitibi-Temiscamingue (UQAT), Val-d'Or, QC J9P 1Y3, Canada

## ARTICLE INFO

### Keywords:

Dual-band

Implantable antenna

ISM

Link budget

Meandered resonator

## ABSTRACT

In this paper, A miniaturized dual-band implantable antenna using meandered line resonator is proposed for bio-telemetry applications. The proposed antenna has dual-band (0.91 GHz and 2.45 GHz) operation, covering the important Industrial, Scientific and Medical (ISM) bands. Miniaturization is achieved using meandered resonator and a square slot etched in the ground plane. The performance of the proposed antenna inside a quasi-implantable biomedical device (IBD) is analysed in a homogeneous skin model, human intestine and human head. The measurements are performed by implanting the quasi-IBD inside a saline solution and minced pork meat. The quasi-IBD consists of the proposed antenna, batteries and printed circuit board (PCB) with electronic components on it. The proposed antenna has compact dimensions of  $5.6 \times 5.8 \times 0.25 \text{ mm}^3$ . The measured peak gains in the minced pork meat are  $-22.9 \text{ dBi}$  and  $-22.1 \text{ dBi}$  at 0.91 GHz and 2.45 GHz, respectively. The low specific absorption rate (SAR) of the proposed antenna allows maximum input power of 3.32 mW at 0.91 GHz and 4.37 mW at 2.45 GHz. To the best of the authors' knowledge, this is the most compact dual-band implantable antenna reported in the literature for 0.91 GHz and 2.45 GHz ISM bands.

## 1. Introduction

Implantable biomedical devices (IBDs) are used in capsule endoscopy [1], cardiac pacemakers [2], intra-oral tongue drive system [3,4], neural recording [5], glucose monitoring [6], intraocular pressure monitoring [7] and many other applications [8]–[9]. Indeed, IBDs are essential for patient monitoring as they collect and transmit information from inside the human body to an outside receiver. In fact, the antenna is a fundamental part of any IBD [10]. Hence, the size of an IBD is proportional to the size of the implantable antenna which consumes more space compared to the other components of the IBD [11–13]. Therefore, miniaturized antenna structures are needed to achieve compact IBDs. In addition, antennas with multi-band operation, large bandwidth, and low SAR value are among other challenges in the design of implantable antennas [14–16].

Recently, several techniques have been reported in the literature to achieve miniaturized and dual-band antennas. Miniaturization approaches include high dielectric substrates [17], slow-wave structures

[18], defected ground structures [19], and reactive loading [20]. However, the bandwidth and gain of the antenna are affected with the miniaturization ratio. Therefore, it is necessary to achieve maximum performance with minimal dimensions. In [20], miniaturization is achieved by generating capacitive effects through meandered slots loading in the radiating patch. Moreover, the dual-band scalp-implantable antenna is designed for intracranial pressure monitoring using meandered line slotting technique for miniaturization [21]. Furthermore, multiple slots in the patch, and an open-ended slot in the ground plane are introduced to design a miniaturized triple-band (405, 915, and 2450 MHz) antenna for skin and deep tissue implantation [22]. In [13], a 37.3% miniaturization ratio is achieved by incorporating triangular patches [23]. In fact, the triangular patches provide additional capacitance and inductance to the radiating patch, and hence, the resonant frequency is shifted to a lower frequencies side. In [21]–[22], meandered resonators are used to miniaturize the size

<sup>☆</sup> This work was supported by the Abu-Dhabi Department of Education and Knowledge (ADEK) Award for Research Excellence 2019 under Grant AARE19-245.

\* Corresponding author.

E-mail addresses: [muath.alhasan@aau.ac.ae](mailto:muath.alhasan@aau.ac.ae) (M. Al-Hasan), [sura.440@gmail.com](mailto:sura.440@gmail.com) (P.R. Sura), [aiqbal@ieee.org](mailto:aiqbal@ieee.org) (A. Iqbal), [jjtiang@mmu.edu.my](mailto:jjtiang@mmu.edu.my) (J.J. Tiang), [ismail.benmabrouk@durham.ac.uk](mailto:ismail.benmabrouk@durham.ac.uk) (I.B. Mabrouk), [mourad.nedil@uqat.ca](mailto:mourad.nedil@uqat.ca) (M. Nedil).

<https://doi.org/10.1016/j.aeue.2021.153896>

Received 10 May 2021; Accepted 9 July 2021

Available online 15 July 2021

1434-8411/© 2021 Elsevier GmbH. All rights reserved.

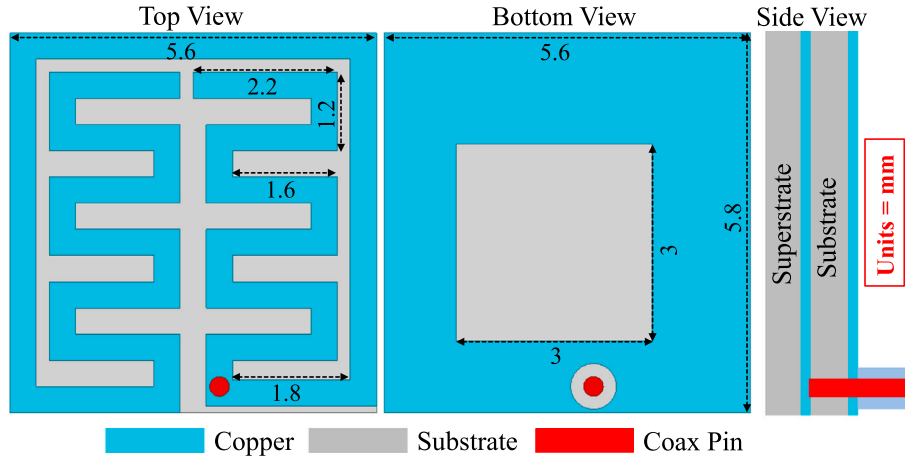


Fig. 1. Geometry of the proposed dual-band implantable antenna.

by increasing the current path. In [24], shorting pins, an open-ended ground plane and reactive elements are loaded to the patch, in order to achieve dual-band operation and miniaturized dimensions. In [25], a dual-band implantable rectenna (402 MHz and 915 MHz) is designed for wireless powering of biomedical implants. In [26], a dual-band implantable antenna is designed at 402 MHz and 2450 MHz ISM bands. Multiple slots on the patch and ground plane are added to realize the targeted frequencies and to achieve miniaturization. In [27], a dual-band antenna is designed using slotted patch, shorting pin and open-ended ground plane. Miniaturization is carried out by utilizing an open-ended slot in the ground plane, with a shorting pin and multiple open-ended slots in the radiating patch. Notwithstanding the dual band characteristics of the above mentioned antenna structures, they have large footprints, low gain, and high SAR values, which are not suitable for IBDs applications. In addition, and to the best of the authors' knowledge, none of them have discussed the design procedure using circuit models.

In this paper, we propose a miniaturized, meandered resonator-based, dual-band implantable antenna for multi-purpose bio-telemetry applications. The proposed antenna operates at 0.91 GHz and 2.45 GHz bands (ISM band), where both bands can be used for telemetry applications. Miniaturization is achieved by increasing the current path through the meandered resonator, square-slot in the ground plane and by using high dielectric substrate. The proposed antenna has a compact geometry of  $5.6 \times 5.8 \times 0.25 \text{ mm}^3 = 8.12 \text{ mm}^3$ . To the best of the authors' knowledge, this is the most compact dual-band implantable antenna reported in the literature for 0.91 GHz and 2.45 GHz ISM bands. Also, the peak gain values of the proposed antenna are higher than other reported dual-band implantable antennas. Moreover, SAR values in both bands are lower than majority of the dual-band implantable antennas. A complete description of the circuit model in each step of the antenna design procedure is also extracted and elaborated.

## 2. Design methodology

### 2.1. Antenna design and system architecture

The layout (top, bottom and side views) of the proposed implantable antenna, along with the associated dimensions are shown in Fig. 1. The proposed antenna has a compact geometry of  $5.6 \times 5.8 \times 0.25 \text{ mm}^3 = 8.12 \text{ mm}^3$ . It exhibits dual-band operation and covers the 0.91 GHz and 2.45 GHz, ISM bands. The proposed antenna incorporates coaxial-fed meandered resonator, and slotted ground plane. Miniaturization is achieved by increasing the current path of the resonator using meandered geometry. Also, the square slot in the ground plane adds additional capacitance effect, which shifts the resonant frequency to a

lower frequency band. The partial ground plane and the meandered resonator are printed on 0.25 mm thick RO3010 ( $\epsilon_r = 10.2$ , and  $\tan \delta = 0.0027$ ) substrate. Another 0.13 mm thick layer of the same material is used as a superstrate. A superstrate, which is considered as dielectric loading [28], is included to achieve additional miniaturization. Moreover, the superstrate protects the radiating element from direct contact with the casing and other components in the IBD. The position of the coaxial cable is parametrically adjusted for better impedance matching ( $50\Omega$ ) at the desired frequency bands. Based on the actual dimensions of the coaxial cable, diameter of the centre core is selected as 0.5 mm and the overall cable is 2 mm. The proposed antenna is designed for bio-telemetry applications using 0.91 GHz and 2.45 GHz ISM bands. In reality, biomedical implantable devices have restricted dimensions. Therefore, implantable antenna should be designed to have minimal dimensions at the targeted frequencies. Meandered resonator is chosen to reduce dimensions of the antenna and to obtain the required radiation patterns. In fact, omni-directional radiation pattern is preferred for bio-telemetry applications. The omni-directional radiation pattern has the advantage to transfer the data in all directions. Therefore, meandered monopole geometry is used in this work.

In real-time practical applications, an implantable antenna always lies inside an IBD, where the architecture varies with applications. Therefore, it is necessary to study the antenna performance in a quasi-real environment by placing the antenna inside a quasi-IBD. In fact, two types of IBDs are considered in the literature for bio-telemetry: (1) capsule-type IBDs for deep-tissue implantation, and (2) flat-type IBDs for skin implantation. In this contribution, both IBDs architectures are considered, as shown in Fig. 2. Both IBDs contain mini-batteries, a PCB with surface mounted devices (SMDs) and the proposed dual-band antenna. IBDs components are enclosed by cylindrical and rectangular biocompatible casings (thickness = 0.25 mm) of alumina ( $\epsilon_r = 9.8$ ).

### 2.2. Simulation environments and measurement setup

Firstly, the proposed antenna is simulated inside a homogeneous skin model ( $100 \times 100 \times 100 \text{ mm}^3$ ), as shown in Fig. 3. The capsule IBD is implanted at a depth of 50 mm and the flat IBD is implanted at a depth of 4 mm in the skin model. The radiation box is designed at a distance of more than  $\lambda/4$  from the edges of the IBD. The permittivity of the skin model is made frequency dependent [29]. The dielectric properties of the tissue are  $\epsilon_r = 41.6$  and  $\sigma = 0.87 \text{ S/m}$  at 0.91 GHz, and  $\epsilon_r = 52.73$  and  $\sigma = 1.74 \text{ S/m}$  at 2.45 GHz [29]. In practical applications, IBDs are implanted in human body, hence, it is necessary to analyse the performance of the antenna in a human model. Thereby, the capsule IBD and the flat IBD are analysed in the intestine and in the head of the human body, respectively.

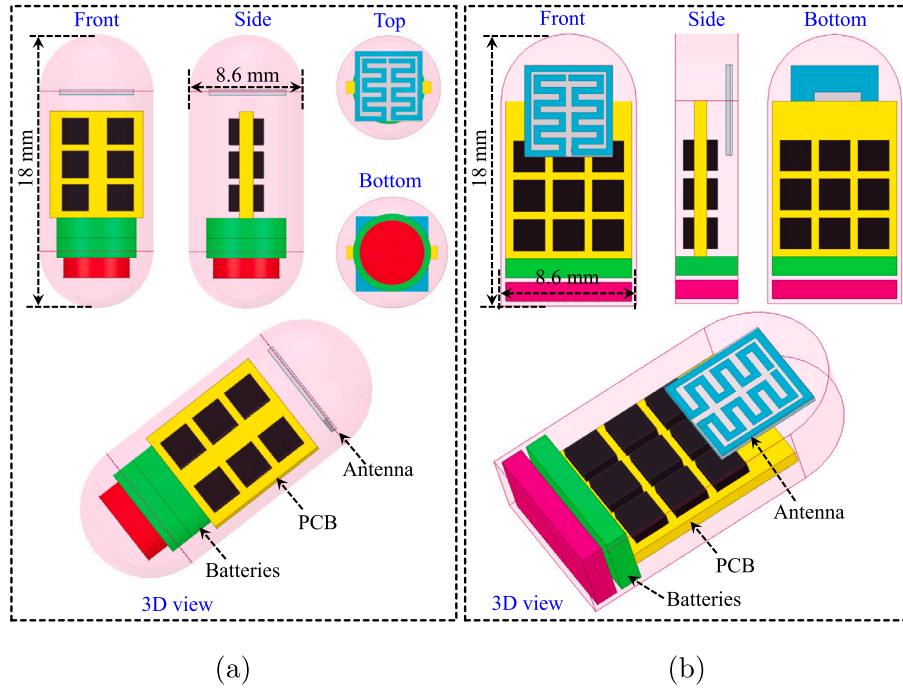


Fig. 2. System architecture of IBD (a) capsule IBD for the deep tissue implantation and (b) flat IBD for the skin implantation.

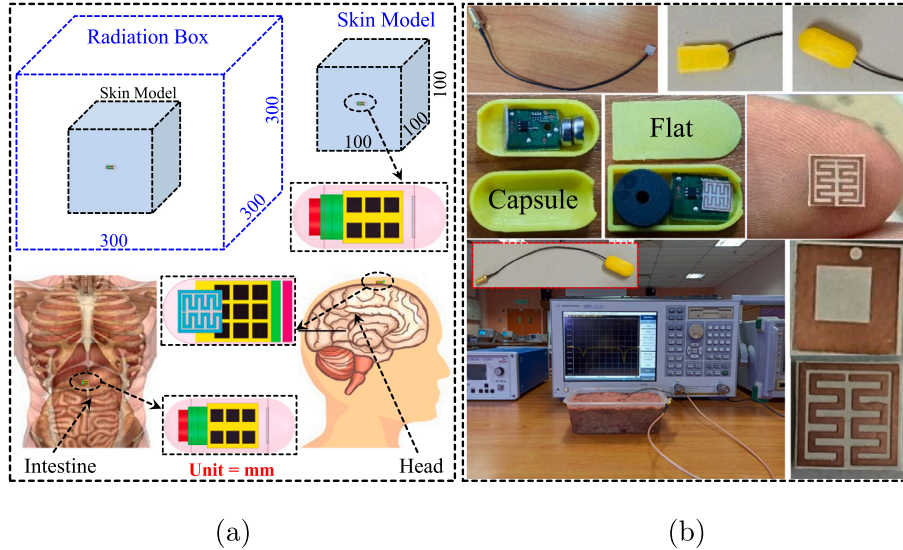


Fig. 3. (a) Analysis setup in the skin, intestine of the human model and head of the human model and (b) fabricated prototype and measurement setups.

A prototype of the proposed dual-band implantable antenna is fabricated using a 0.25 mm thick RO3010 substrate ( $\epsilon_r = 10.2$ , and  $\tan\delta = 0.0027$ ) to validate the simulated results. Quasi-IBDs are fabricated using 3D printing technology. The PCB is fabricated on a 1 mm thick FR-4 substrate. Different types of SMDs are soldered over the PCB. The PCB, mini-batteries, antenna element, and superstrate are embedded inside the IBDs. In simulations, silver material is assigned to batteries and FR-4 material is assigned to PCB. Each battery has radius of 3 mm and height of 1.5 mm. The PCB has dimensions of  $7 \times 9 \times 1 \text{ mm}^3$ . Properties of resistors (1 K $\Omega$ ), inductors (1 nH) and capacitors (1 pF) are assigned to black boxes on the PCB. It is worth mentioning that these values are only for demonstration purpose and any value could be used. Each box on the PCB has dimensions of  $2 \times 2 \times 1 \text{ mm}^3$ . The lid/cap of IBDs is fixed over the container using epoxy. The reflection coefficient of the antenna is measured in a minced pork meat and a

saline solution and the radiation pattern of the antenna is measured in a minced pork meat. The fabricated prototype, the 3D printed capsule-IBD and the flat-IBD are illustrated in Fig. 3(b). Moreover, the reflection coefficient and radiation pattern measurement setup are also shown in Fig. 3(b).

### 2.3. Design evolution steps and lumped element equivalent circuit models

The proposed antenna is optimized in three steps, where the results, descriptions of electromagnetic (EM) and circuit models are given in each step. First, the design process is initiated by designing a simple  $\lambda/2$  monopole radiator. Eq. (1) is used to estimate the length of the monopole radiator. The meandered resonator is designed on the right-hand side of the substrate. The meandered geometry of the radiator is chosen to keep a large current path in limited space. The large current

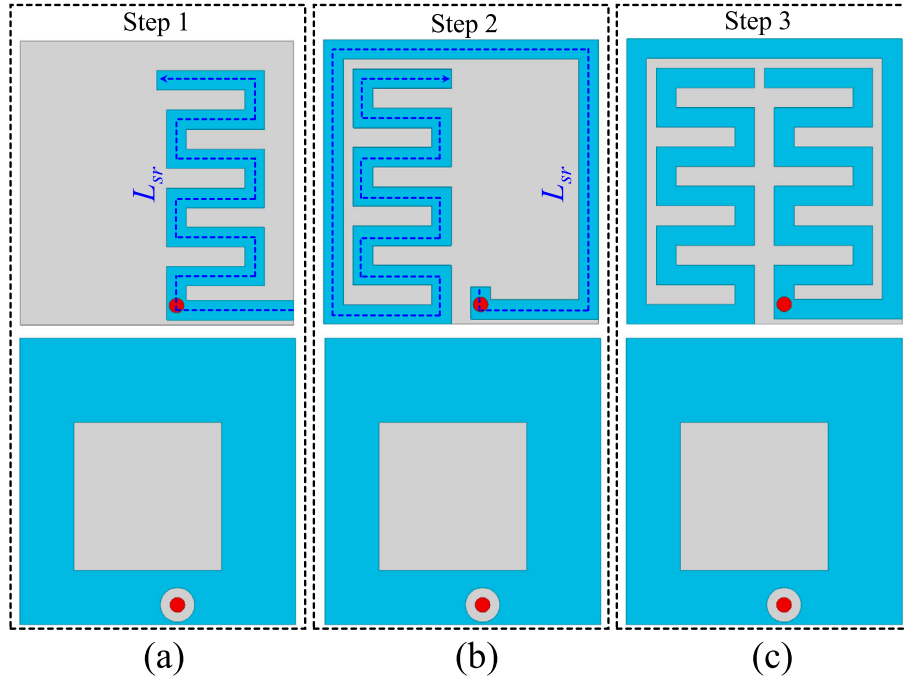


Fig. 4. Evolution stages of the proposed antenna (a) step 1, (b) step 2 and (c) proposed dual-band antenna (0.91 and 2.45 GHz).

path enables the antenna to operate at lower frequency, and hence miniaturization is achieved (see Fig. 4).

$$L_{sr} = \frac{c}{2 \times f \sqrt{\epsilon_r}} \quad (1)$$

where  $L_{sr}$  is the effective length of the meandered radiator,  $c$  is the speed of light and  $f$  is the operating frequency. At 2.4 GHz, the resonator length ( $L_{sr}$ ) is calculated as 19 mm. With this length, the antenna resonates at 2.8 GHz because the effective radiating area of the meandered monopole is less than the actual physical length. Unlike the conventional full ground plane, a square-slotted ground is adopted for miniaturization. The slot in the ground plane provides additional capacitance to the antenna. According to Eq. (2), the resonant frequency depends on the equivalent capacitance and inductance of the antenna [18]. As a result, increase in the capacitance and the inductance lead the antenna to operate at lower frequencies. In the proposed design, the antenna compactness is improved by increasing the total capacitance, and thus, the antenna resonates at a lower frequency than its fundamental frequency. In the first step, the antenna resonates at 2.8 GHz. The physical dimensions are calculated at 2.4 GHz. However, the effective length of the radiator is lower than the actual physical length and hence, the antenna resonates at 2.8 GHz instead of 2.4 GHz. The lumped equivalent circuit model is extracted for the resonator in the first step. It is known that a single resonator can be modelled as a parallel RLC circuit [30]. The impedance transformer can be used to couple the source with the load. The same concept is used to model the proposed monopole radiator. The circuit is modelled and optimized using the Keysight Advance Design System (ADS). The reflection coefficient results of both EM and circuit models are compared in Fig. 5(a).

$$v_p = \frac{1}{\sqrt{LC}} = \frac{c}{\sqrt{\epsilon_{eff}}} = \lambda_g f \quad (2)$$

where  $v_p$  is the wave propagation velocity,  $L$  is the total inductance of the antenna,  $C$  is the total capacitance of the antenna,  $\epsilon_{eff}$  is the relative permittivity of the substrate, and  $\lambda_g$  is the guided wavelength at the resonant frequency ( $f$ ).

Second, the length of the meandered monopole radiator is increased, where, the current path is increased with the length of the meandered resonator. In this step, the length of the meandered monopole

radiator is calculated at 0.915 GHz using Eq. (1). At 0.91 GHz, the resonator length ( $L_{sr}$ ) is calculated as 51 mm. With this length, the fundamental mode ( $TM_{10}$ ) of the antenna is excited at 1.2 GHz. The resonant frequency occurred at the higher frequency band, because the effective length of the meandered radiator is less than that of the calculated one. The equivalent lumped element circuit is modelled, and the circuit values are extracted, as shown in Fig. 5(b). The reflection coefficient of the EM and circuit model is compared in Fig. 5(b).

Finally, the resonators of the first and second steps are combined to design a dual-band (0.91 GHz, and 2.45 GHz) antenna. In this step, the antenna resonates at 0.91 GHz and 2.4 GHz. The equivalent circuit model is shown in Fig. 5(c), where each resonator is modelled as an RLC circuit and the coupling between the two resonating modes ( $TM_{10}$  and perturb  $TM_{10}$ ) is modelled as a series LC circuit [31]. The reflection coefficient from the EM and circuit model simulation is shown in Fig. 5(c). The loaded quality factor of the first band of the monopole is given by Eq. (3) [32].

$$Q_{L1} = \frac{R_{T1}}{\omega_o L} = \frac{f_o}{f - 90 - f + 90} \quad (3)$$

where  $Q_{L1}$  is the loaded quality factor of the first resonant band,  $R_{T1}$  is the equivalent resistance of the parallel RLC circuit of the first resonant band,  $\omega_o$  is the angular frequency,  $L$  is the inductance of first resonant band,  $f_o$  is the resonant frequency obtained from the peak of the group delay and  $f^{\pm 90}$  is the lower and upper shift of 90° from  $f_o$  on the phase curve of  $S_{11}$ . The quality factor in the EM model can be adjusted by changing the position of the coaxial probe. It is known that the monopole is directly coupled with the source through a 50Ω coaxial probe. Thus, the coupling phenomenon between the source and load can be estimated through Eq. (4) [32].

$$K_{s1} = \sqrt{\left( \frac{1}{R_{T1}} - \frac{1}{R_1} \right) Z} \quad (4)$$

where  $K_{s1}$  is the coupling between the source and the first resonant mode of the monopole antenna,  $R_{T1}$  is the total resistance of the parallel RLC circuit and  $Z$  is the input impedance. Using Eq. (4), coupling between the source and the first mode ( $K_{s1}$ ) is noted as 0.407.

The second resonant mode (perturb  $TM_{10}$ ) of the monopole is coupled to the first resonant mode of the monopole, as depicted in

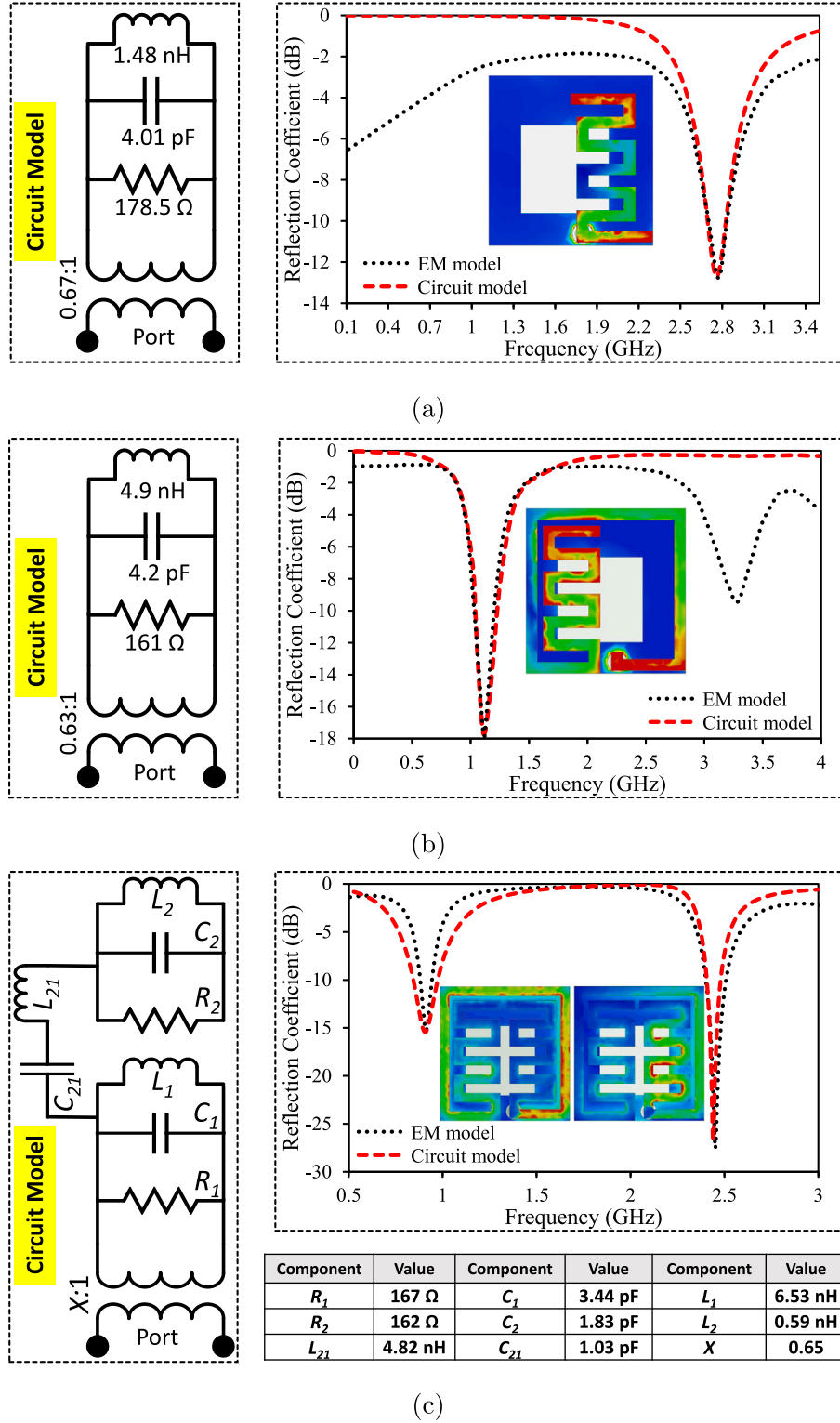


Fig. 5. Simulated (EM and circuit model) reflection coefficient results in (a) step 1, (b) step 2 and (c) step 3.

Fig. 5(c). The first resonant mode is directly coupled to the source, whereas the second resonant mode is coupled to the first resonant mode and the source impedance. Since the second resonant mode is operating at higher frequency than the first resonant mode, it has minimal loading effect on the first resonant mode. Therefore, the first resonant mode of the monopole is considered as a coupling agent for the second resonant mode. The loaded quality factor of the second resonant mode of the

monopole radiator is given by Eq. (5).

$$Q_{L2} = \frac{R_{T2}}{\omega_o L} = \frac{f_o}{f - 90 - f + 90} \quad (5)$$

where  $Q_{L2}$  is the loaded quality factor of the second resonant mode,  $R_{T2}$  is the equivalent resistance of the parallel RLC circuit of the second resonant mode and  $L$  is the inductance of the second resonant mode. The quality factor of the second resonant mode also depends on the



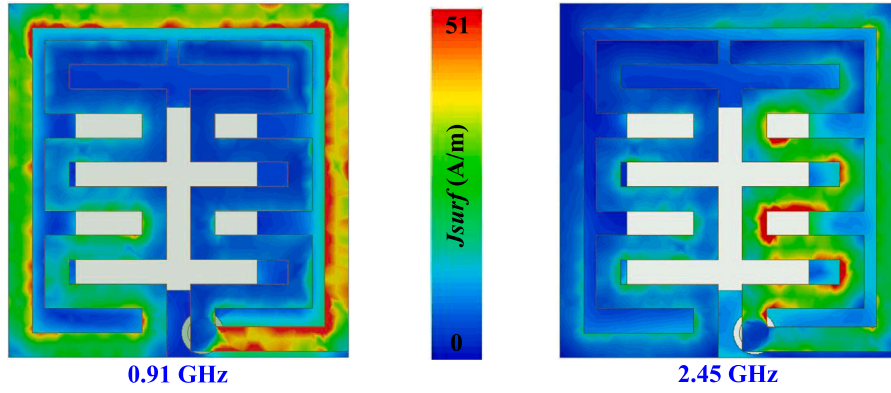


Fig. 6. Surface current distribution on the patch and ground at 0.91 and 2.45 GHz.

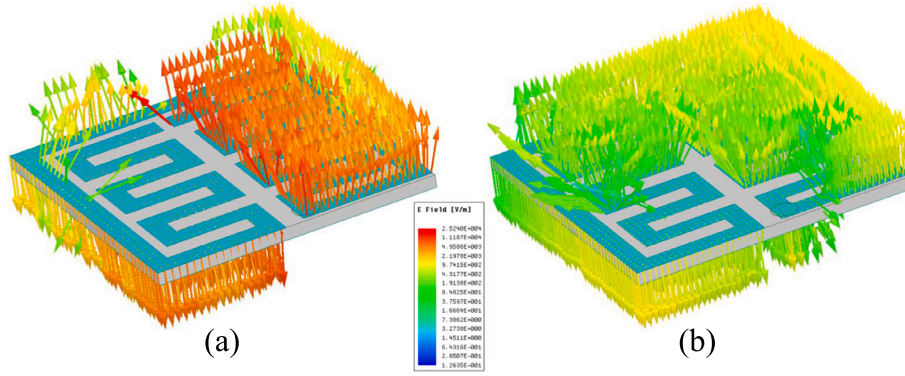


Fig. 7. Electric field distribution of the radiating patch at (a) 0.91 GHz and (b) 2.45 GHz.

position of the coaxial probe. The simulated quality factors (from filter theory) of the two resonant modes are 15.1 and 10.2, respectively. The quality factor is inversely proportional to the bandwidth, which decreases with the increase in the bandwidth. The bandwidth of the first resonant band is lower than that of the second one. Therefore, it has higher quality factor than the second band.

The coupling phenomenon of the resonant mode 2 with the resonant mode 1 and the source is given by Eq. (6).

$$K_{s21} = \sqrt{\left(\frac{1}{R_{T2}} - \frac{1}{R_2}\right) Z_{eq}} \quad (6)$$

$K_{s21}$  is the coupling between the second resonant mode of the monopole antenna with the source and the first resonant mode.  $Z_{eq}$  represents the equivalent impedance of the source and the first resonant mode. Using Eq. (6), coupling between the source and the first mode with the second mode ( $K_{s21}$ ) is noted as 1.87.

#### 2.4. Fields distribution

Fig. 6 shows the surface current distribution on the patch and ground plane at 0.91 GHz and 2.45 GHz. It can be noticed that the current distribution (see Fig. 6) has a high concentration on the right side of the resonator in both resonant modes. The region on the resonator, which has a high concentration in both resonant modes, illustrates the coupling between the both resonant modes. Fig. 7 shows electric field distribution of the antenna at 0.91 GHz and 2.45 GHz. At 0.91 GHz, the electric field varies once and is odd symmetrical. Therefore,  $TM_{10}$  mode is excited at this frequency. At 2.45 GHz, the electric field also varies once but is not perfectly odd symmetrical. In fact, the electric field distribution is disturbed, as shown in Fig. 7b. The electric field almost follows the pattern of  $TM_{10}$  mode. Therefore, perturb  $TM_{10}$  mode is identified at this frequency.

#### 2.5. Impact of the PCB on the antenna

Implantable medical devices are always integrated inside a device containing a PCB, RF components and electrical components. Since majority of these components are made of conducting materials, hence couple with an antenna. Consequently, affect impedance matching and radiation properties of an antenna. It is important to place an antenna in a device to have limited coupling. To find an optimum place of the proposed antenna, a parametric analysis is performed in both devices, as shown in Fig. 8. It can be observed that the impedance is effected with decrease in the separation distance ( $h$ ). To have better impedance matching at the desired frequencies, a minimum separation gap ( $h$ ) of 1 mm and 1.4 mm is required in capsule-type and flat-type device, respectively.

### 3. Simulation and experimental results

A simple meandered radiator, embedded with dummy electronic components and batteries, is considered in the antenna design. Then, the antenna is enclosed in the flat and capsule IBD, where the integrated antenna system is simulated at the centre of a homogeneous skin model ( $100 \times 100 \times 100 \text{ mm}^3$ ). Parameters of the initially designed antenna are optimized to get the desired bands. Then, the antenna is simulated inside a human model. In this study, simulation of the flat IBD is performed in the head of a human model and capsule IBD in the intestine of a human model. The simulation setups of the three simulations scenarios are shown in Fig. 3. The simulation results are practically validated by testing both IBDs in the minced pork meat and saline solution. The antenna is prototyped on a high dielectric material of Rogers RO3010 ( $\epsilon_r = 10.2$ ,  $\tan\delta = 0.0027$ ), and the casings of IBDs are fabricated using 3D printing technology. The antenna, the batteries and the PCB are placed inside IBDs. Different electronic components

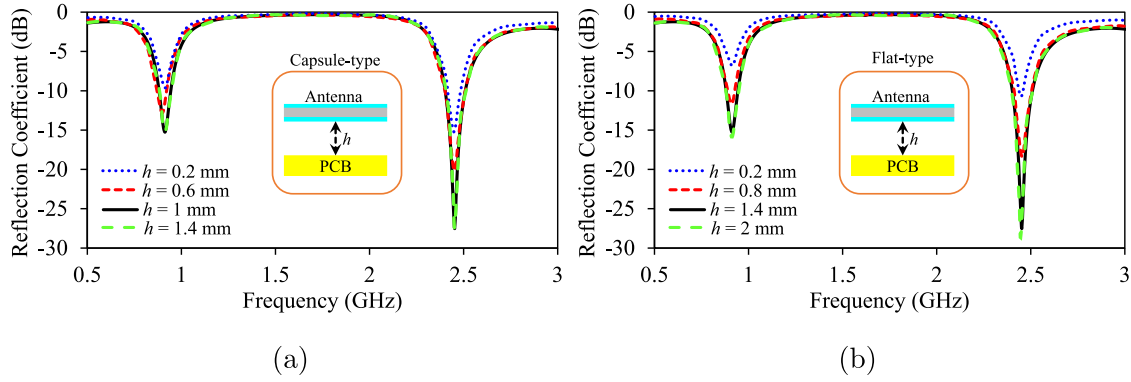


Fig. 8. Influence of the PCB on the impedance matching of the antenna (a) capsule-type device, and (b) flat-type device.

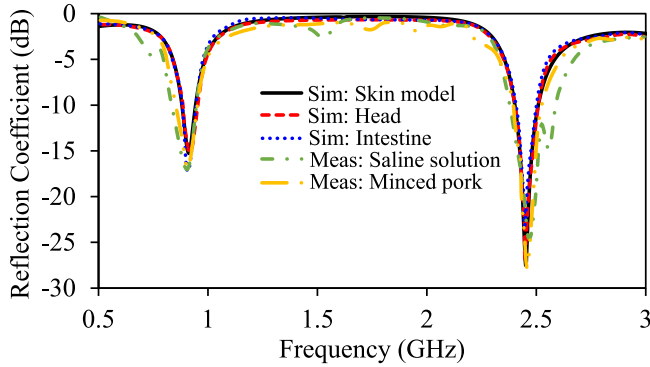


Fig. 9. Simulated and measured reflection coefficient of the antenna.

(SMDs) are soldered over the PCB. IBDs are carefully closed with epoxy to prevent any leaks during the practical measurements. The reflection coefficient is measured in the minced pork meat and saline solution. The radiation patterns are only measured in the minced pork meat. The fabricated prototypes of the antenna, IBDs and measurement setups are illustrated in Fig. 3(b).

Furthermore, the simulated and measured reflection coefficients of the antenna are plotted in Fig. 9. It is observed, from the simulated and measured data, that the antenna operates at two frequency bands. The simulations are performed in a homogeneous skin model, intestine of the human model and head of the human model. The measurements are carried out in the minced pork meat and saline solution. Initially, ingredients of the saline solution are estimated for lower frequency band to measure the lower frequency band followed by making the solution for high frequency band. The ingredients of the saline solution at the lower frequency band contain 72% water, 1.35% salt and 56.5% sugar by weight [23]. Similarly, the ingredients of the saline solution at the higher frequency band contain 72% water, 23% diethylene glycol butyl ether, and 5% Triton X-100 [33]. Both results are combined and shown in Fig. 9. It can be seen that the resonant frequencies and operational bandwidth in all simulation scenarios are almost the same. The antenna has resonances at 0.91 and 2.45 GHz with corresponding 10-dB bandwidths of 94 MHz (0.865–0.959 GHz) and 160 MHz (2.37–2.53 GHz), respectively. A negligible shift (5–8 MHz) in the simulated resonant frequencies of both bands is noticed in the intestine and head of the human model due to different implantation depth. It is worthy mentioning that the proposed antenna is simulated using HFSS, where human phantom is available. In fact, the properties of the human phantom are pre-defined and same for all parts of the body. Therefore, negligible shift is noticed in all simulations. A small frequency shift in the lower and high band is observed in the practical measurements. It may be mainly due to: (1) fabrication imperfection

Table 1

Important parameters for the link budget analysis.

Variables	Description (Units)	Values
$f$	Frequency (GHz)	0.91 and 2.45
$P_t$	Transmitted power (dBm)	-16
$G_t$	Implantable antenna gain (dBi)	-23.74 and -21.6
$G_r$	Receiver antenna gain (dBi)	2
$\gamma$	Path loss exponent	1.5
$X_\sigma$	Shadowing factor	4
$d$	Distance (m)	Variable
$L_f$	Feed losses (dB)	2.3
$L_p$	Polarization loss (dB)	0.5

and cable losses, (2) air gap between the antenna and superstrate and (3) difference in electrical properties of the minced meat pork, saline solution and simulation environments. Multiple resonances and broader 10-dB operational bandwidth are noticed by measuring the antenna in the saline solution. The discrepancy in the results may be attributed to the imperfection of the saline solution properties. The bandwidths in all scenarios (simulated and measured) are good enough to cover the targeted ISM bands (0.91 and 2.45 GHz).

The simulated and measured radiation patterns of the antenna in  $\phi = 0^\circ$  and  $\phi = 90^\circ$  planes at 0.91 and 2.45 GHz are shown in Fig. 10. The simulated radiation pattern of the homogeneous skin model and measured radiation pattern in the minced pork meat is considered in this paper. For measurements, the minced pork meat is packed inside a polythene bag, where the antenna system is kept inside. A high gain horn antenna is used as a transmitter in the anechoic chamber and the antenna (inside the packed minced pork meat) is considered as a receiving antenna. The high gain horn antenna remains stationary and the minced pork meat is rotated in both planes to record the received power. A good agreement between the simulated and the measured results is achieved as illustrated from Fig. 10. The measured peak gains of -22.9 dBi at 0.91 GHz and -22.1 dBi at 2.45 GHz in the minced pork are noted.

The specific absorption rate (SAR) is evaluated over a 1-g of tissue to ensure the user safety. In this work, the SAR distribution is analysed by placing the antenna inside the intestine and head of the human model. The peak SAR distributions at 0.91 and 2.45 GHz inside the human model (intestine and head) are shown in Fig. 11. The peak SAR values of 481.1 W/Kg at 0.91 GHz in the intestine, 365.3 W/Kg at 2.45 GHz in the intestine, 449.9 W/Kg at 0.91 GHz in the head and 312.7 W/Kg at 2.45 GHz in the head are noted when the input power is 1 W. It is also observed that the peak SAR values are higher at the lower frequency band than the upper ones. The lower frequency band has a larger wavelength as compared to the upper frequency band, which can easily penetrate the tissues and thus has a high SAR value. Moreover, it is observed from the current distribution plot of the antenna that the lower frequency band has a high current concentration on the

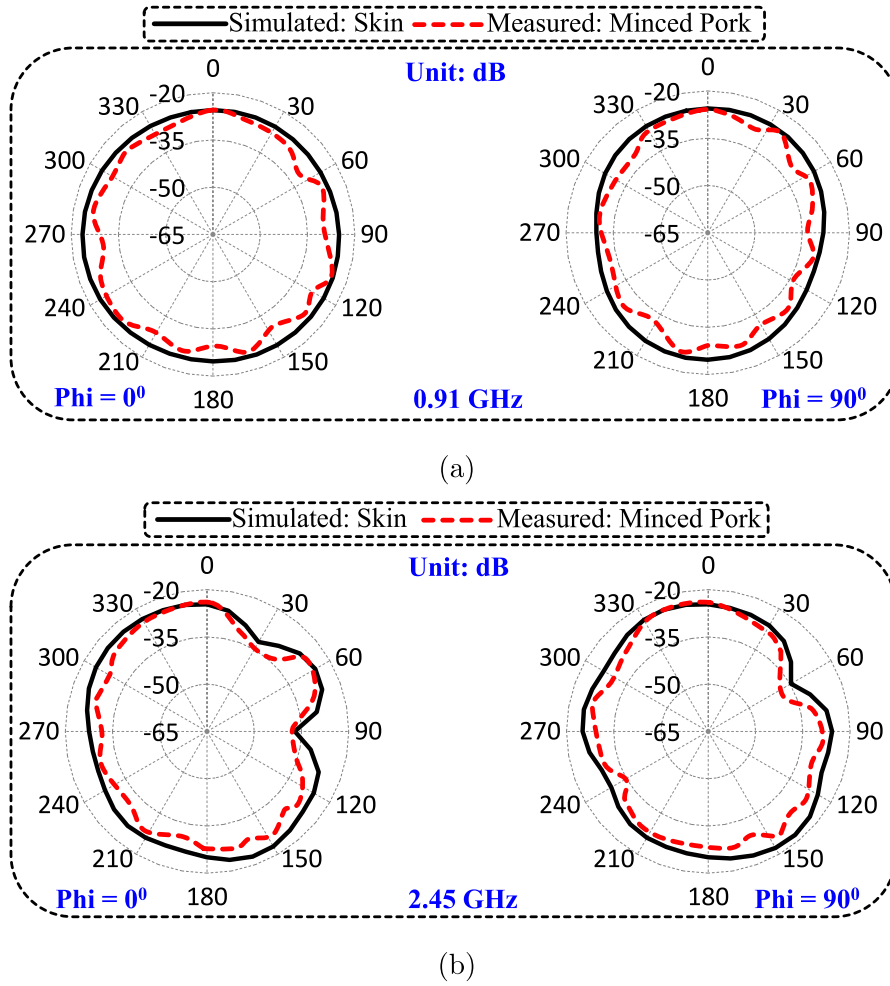


Fig. 10. Simulated (homogeneous skin model) and measured (minced pork) radiation pattern of the antenna at (a) 0.91 GHz and (b) 2.45 GHz.

larger part of the radiator than the upper band. This phenomenon also attributes to the larger SAR values at the lower frequency band. According to the standards provided by the IEEE, the SAR value must be less than 1.6 W/Kg for the input power of 1 W. The simulated peak SAR values seem to be high as compared to the standard imposed by the IEEE. However, the maximum input power for IBDs is restricted to 25  $\mu$ W [34]. To keep the SAR values under the IEEE standards, the proposed antenna allows maximum input power of 3.32 mW at 0.91 GHz (lower frequency band) and 4.37 mW at 2.45 GHz (upper frequency band). Based on the restricted input power of 25  $\mu$ W, the proposed antenna is safe for the operation in both bands.

Indeed, an efficient and reliable communication link between the internal IBD and external receiver is important for real-time bio-telemetry. In fact, different losses such as path losses, feed losses, antenna mismatch losses, polarization losses, path loss exponent ( $\gamma$ ) and dielectric losses affect the communication link. The Friis transmission equation is used to theoretically analyse the communication ability of the system. The important parameters are listed in Table 1. The following relationship is used to derive theoretical results.

$$P_r[dB] = G_t + G_r + P_i + 20 \log \left( \frac{\lambda}{4\pi d} \right) \quad (7)$$

The theoretical results are practically verified by real-time communication using two software-defined radio (SDR) platforms. One SDR is connected with the IBD and the other SDR with the monopole antenna. An audio signal of 15 MHz bandwidth is generated using the transmitting SDR and transmitted through the IBD using frequency modulation scheme. The monopole antenna is placed at a distance

(d) to receive the incoming signal. The receiving SDR is connected to a PC to record the strength of the incoming signal. The setup for the practical measurements is shown in Fig. 12. The theoretical and practical received powers are compared and presented in Fig. 12. The practical demonstration confirms that the proposed antenna is suitable for real-time bio-telemetry in both bands.

A detailed comparison of the proposed antenna with multi-purpose dual-band implantable antennas, reported in literature, is also presented in Table 2. It is noticeable that the proposed antenna has the best compactness and higher gains than the reported dual-band implantable antennas. Moreover, a circuit model of the proposed antenna system is developed to show the real behaviour of the excited modes. None of the antennas in reported literature show circuit model of the excited modes. Also, SAR values in both bands are better than the majority of the reported dual-band antennas.

#### 4. Conclusion

In this paper, a low profile dual-band implantable antenna based on meandered resonator is developed and experimentally validated. Miniaturization is achieved by adding a square-slot in the ground plane and using meandered resonator. An efficient circuit model of the proposed antenna system is developed to investigate the real behaviour of the excited modes. It has been demonstrated that both excited modes are inter-dependent and are not freely adjustable. The proposed antenna operates at 0.91 GHz and 2.45 GHz with 10-dB bandwidths of 94 MHz and 160 MHz, respectively. The fabricated antenna has compact dimensions of  $5.6 \times 5.8 \times 0.25$  mm<sup>3</sup>. The measured gains in



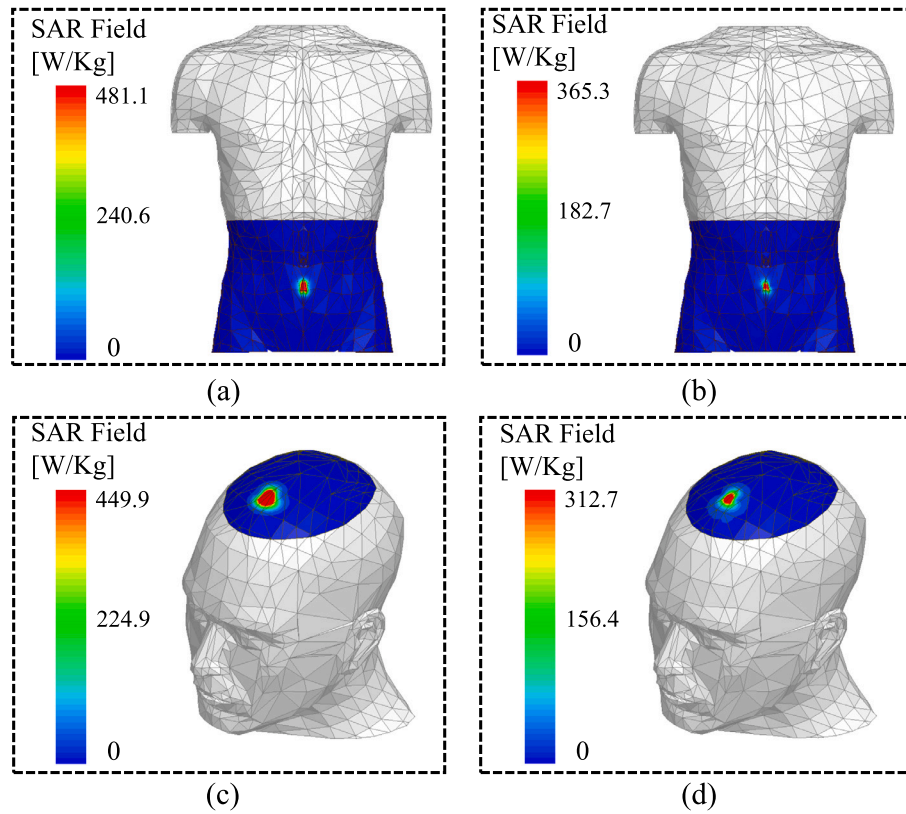


Fig. 11. 1-g SAR distribution at an input power of 1 W (a) human intestine at 0.91 GHz, (b) human intestine at 2.4 GHz, (c) human head at 0.91 GHz and (d) human head at 2.4 GHz.

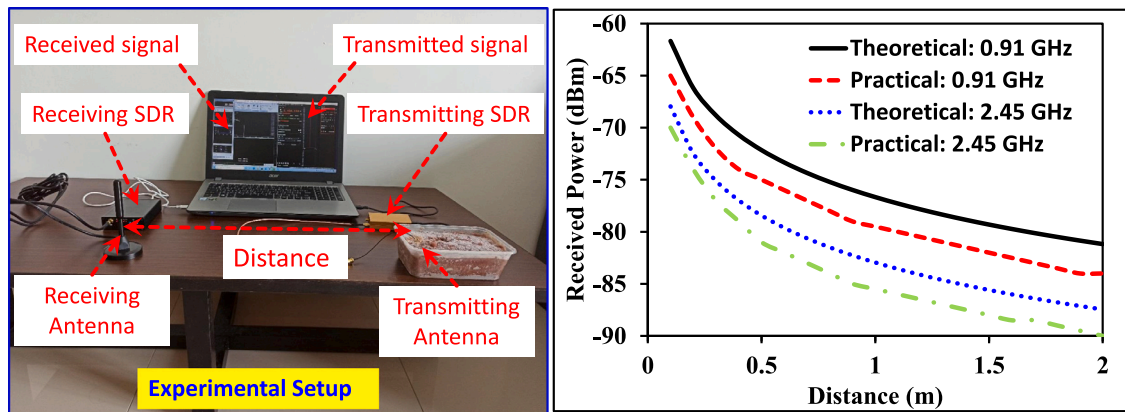


Fig. 12. Theoretical and practical results of the communication link and experimental setup.

Table 2

Comparison with the dual-band implantable antennas.

Ref.	Size ( $\lambda_g^3$ )	Size (mm <sup>3</sup> )	Frequency (GHz)	Bandwidth (MHz)	Gain (dBi)	SAR (W/Kg)	Implant depth
[6]*	$0.09 \times 0.09 \times 0.01$	$22.5 \times 22.5 \times 2.5$	0.402/2.4	82/100	–	–	–
[9]	$0.07 \times 0.06 \times 0.002$	$7 \times 6 \times 0.254$	0.91/2.45	84/144	–17.1/–9.81	576.1/524.3	50 mm
[10]*	$0.09 \times 0.1 \times 0.005$	$22 \times 23 \times 1.27$	0.402/2.45	30/168	–36.7/–27.1	832/690	4 mm
[16]	$0.07 \times 0.07 \times 0.0004$	$6.5 \times 6.5 \times 0.05$	0.915/2.45	123.5/154.4	–28.2/–24.5	420.3/233.2	50 mm
[21]	$0.08 \times 0.06 \times 0.004$	$8 \times 6 \times 0.5$	0.915/2.45	90/210	–25.5/–22.8	971/807	4 mm
[24]*	$0.07 \times 0.07 \times 0.002$	$7 \times 7.2 \times 0.2$	0.928/2.45	184.1/219.7	–28.74/–25.65	471/313	50 mm
[27]	$0.07 \times 0.07 \times 0.002$	$7 \times 7 \times 0.2$	0.915/2.45	107.5/560	–27.65/–22.99	730.07/591.40	50 mm
This work	$0.05 \times 0.05 \times 0.002$	$5.6 \times 5.8 \times 0.25$	0.91/2.45	94/160	–23.74/–21.6	481.1/365.3	50 mm

$\lambda_g$  is the guided wavelength at the lower resonant band (only relative permittivity of substrates is considered for calculating guided wavelength), \* represent implantable antennas without considering them in implantable device. SAR is presented for an input power of 1 W.

the minced pork meat are  $-22.9$  dBi and  $-22.1$  dBi at  $0.91$  GHz and  $2.45$  GHz, respectively. Moreover, the proposed antenna has low SAR values at both bands and allow maximum input power of  $3.32$  mW at the lower frequency band and  $4.37$  mW at the higher frequency band. The reliability of communication link is practically demonstrated, which confirms that the proposed antenna is suitable for a real-time bio-telemetry in both bands.

### Declaration of competing interest

The authors declare that they have no known competing financial interests or personal relationships that could have appeared to influence the work reported in this paper.

### References

- [1] Bao Z, Guo Y-X. Novel miniaturized antenna with a highly-tunable complex input impedance for capsules. *IEEE Trans Antennas and Propagation* 2020.
- [2] Asif SM, Iftikhar A, Braaten BD, Ewert DL, Maile K. A wide-band tissue numerical model for deeply implantable antennas for RF-powered leadless pacemakers. *IEEE Access* 2019;7:31031–42.
- [3] Kong F, Zada M, Yoo H, Ghovanloo M. Adaptive matching transmitter with dual-band antenna for intraoral tongue drive system. *IEEE Trans Biomed Circuits Syst* 2018;12(6):1279–88.
- [4] Kong F, Qi C, Lee H, Durgin GD, Ghovanloo M. Antennas for intraoral tongue drive system at  $2.4$  GHz: Design, characterization, and comparison. *IEEE Trans Microw Theory Tech* 2018;66(5):2546–55.
- [5] Bahrami H, Mirbozorgi SA, Ameli R, Rusch LA, Gosselin B. Flexible, polarization-diverse UWB antennas for implantable neural recording systems. *IEEE Trans Biomed Circuits Syst* 2015;10(1):38–48.
- [6] Karacolak T, Hood AZ, Topsakal E. Design of a dual-band implantable antenna and development of skin mimicking gels for continuous glucose monitoring. *IEEE Trans Microw Theory Tech* 2008;56(4):1001–8.
- [7] Bhamra H, Tsai J-W, Huang Y-W, Yuan Q, Shah JV, Irazoqui P. A subcubic millimeter wireless implantable intraocular pressure monitor microsystem. *IEEE Trans Biomed Circuits Syst* 2017;11(6):1204–15.
- [8] Nikolayev D, Zhadobov M, Sauleau R. Immune-to-detuning wireless in-body platform for versatile biotelemetry applications. *IEEE Trans Biomed Circuits Syst* 2019;13(2):403–12.
- [9] Zada M, Shah IA, Yoo H. Metamaterial-loaded compact high-gain dual-band circularly polarized implantable antenna system for multiple biomedical applications. *IEEE Trans Antennas and Propagation* 2019;68(2):1140–4.
- [10] Liu Y, Chen Y, Lin H, Juwono FH. A novel differentially fed compact dual-band implantable antenna for biotelemetry applications. *IEEE Antennas Wirel Propag Lett* 2016;15:1791–4.
- [11] Kumar SA, Shanmuganantham T. Design of implantable CPW fed monopole H-slot antenna for  $2.45$  GHz ISM band applications. *AEU-Int J Electron Commun* 2014;68(7):661–6.
- [12] Basir A, Zada M, Cho Y, Yoo H. A dual-circular-polarized endoscopic antenna with wideband characteristics and wireless Biotelemetric link characterization. *IEEE Trans Antennas and Propagation* 2020.
- [13] Kumar SA, Shanmuganantham T. Design and analysis of implantable CPW fed bowtie antenna for ISM band applications. *AEU-Int J Electron Commun* 2014;68(2):158–65.
- [14] Kiourti A, Nikita KS. Miniature scalp-implantable antennas for telemetry in the MICS and ISM bands: Design, safety considerations and link budget analysis. *IEEE Trans Antennas and Propagation* 2012;60(8):3568–75.
- [15] Xu L-J, Bo Y, Lu W-J, Zhu L, Guo C-F. Circularly polarized annular ring antenna with wide axial-ratio bandwidth for biomedical applications. *IEEE Access* 2019;7:59999–60009.
- [16] Hayat S, Shah SAA, Yoo H. Miniaturized dual-band circularly polarized implantable antenna for capsule endoscopic system. *IEEE Trans Antennas and Propagation* 2020.
- [17] Tang X, Wong H, Long Y, Xue Q, Lau K. Circularly polarized shorted patch antenna on high permittivity substrate with wideband. *IEEE Trans Antennas and Propagation* 2011;60(3):1588–92.
- [18] Chi P-L, Waterhouse R, Itoh T. Antenna miniaturization using slow wave enhancement factor from loaded transmission line models. *IEEE Trans Antennas and Propagation* 2010;59(1):48–57.
- [19] Banerjee U, Karmakar A, Saha A, Chakraborty P. A CPW-fed compact monopole antenna with defected ground structure and modified parasitic hilbert strip having wideband circular polarization. *AEU-Int J Electron Commun* 2019;110:152831.
- [20] Liu C, Guo Y-X, Xiao S. Capacitively loaded circularly polarized implantable patch antenna for ISM band biomedical applications. *IEEE Trans Antennas and Propagation* 2014;62(5):2407–17.
- [21] Shah SAA, Yoo H. Scalp-implantable antenna systems for intracranial pressure monitoring. *IEEE Trans Antennas and Propagation* 2018;66(4):2170–3.
- [22] Gani I, Yoo H. Multi-band antenna system for skin implant. *IEEE Microw Wirel Compon Lett* 2016;26(4):294–6.
- [23] Zhang Y, Liu C, Liu X, Zhang K, Yang X. A wideband circularly polarized implantable antenna for  $915$  MHz ISM-band biotelemetry devices. *IEEE Antennas Wirel Propag Lett* 2018;17(8):1473–7.
- [24] Faisal F, Yoo H. A miniaturized novel-shape dual-band antenna for implantable applications. *IEEE Trans Antennas and Propagation* 2018;67(2):774–83.
- [25] Ding S, Koulouridis S, Pichon L. Implantable wireless transmission rectenna system for biomedical wireless applications. *IEEE Access* 2020;8:195551–8.
- [26] Ganeshwaran N, Jeyaprakash JK, Alsath MGN, Sathyanarayanan V. Design of a dual-band circular implantable antenna for biomedical applications. *IEEE Antennas Wirel Propag Lett* 2019;19(1):119–23.
- [27] Faisal F, Zada M, Ejaz A, Amin Y, Ullah S, Yoo H. A miniaturized dual-band implantable antenna system for medical applications. *IEEE Trans Antennas and Propagation* 2019;68(2):1161–5.
- [28] Fan Y, Huang J, Chang T, Liu X. A miniaturized four-element MIMO antenna with EBG for implantable medical devices. *IEEE J Electromagn RF Microw Med Biol* 2018;2(4):226–33.
- [29] Gabriel S, Lau R, Gabriel C. The dielectric properties of biological tissues: II. Measurements in the frequency range  $10$  Hz to  $20$  GHz. *Phys Med Biol* 1996;41(11):2251.
- [30] Naeem U, Bila S, Thévenot M, Arnaud E. Design methodology for dual-band hybrid antennas with off-resonance loading. *IET Microw Antennas Propag* 2017;11(14):2077–82.
- [31] Alibakhshienari M, Virdee BS, See CH, Abd-Alhameed R, Ali AH, Falcone F, et al. Study on isolation improvement between closely-packed patch antenna arrays based on fractal metamaterial electromagnetic bandgap structures. *IET Microw Antennas Propag* 2018;12(14):2241–7.
- [32] Hong J-SG, Lancaster MJ. Microstrip filters for RF/microwave applications. 167, John Wiley & Sons; 2004.
- [33] Li R, Guo Y-X, Du G. A conformal circularly polarized antenna for wireless capsule endoscope systems. *IEEE Trans Antennas and Propagation* 2018;66(4):2119–24.
- [34] Basir A, Yoo H. A stable impedance-matched ultrawideband antenna system mitigating detuning effects for multiple biotelemetric applications. *IEEE Trans Antennas and Propagation* 2019;67(5):3416–21.